nature energy

SUPPLEMENTARY INFORMATION

VOLUME: 2 | ARTICLE NUMBER: 17086

In the format provided by the authors and unedited.

Enhanced selectivity in mixed matrix membranes for CO_2 capture through efficient dispersion of amine-functionalized MOF nanoparticles

Behnam Ghalei, [a] Kento Sakurai, [ab] Yosuke Kinoshita, [ab] Kazuki Wakimoto, [ab] Ali Pournaghshband Isfahani, [a] Qilei Song, [c] Kazuki Doitomi, [d,e] Shuhei Furukawa, [a] Hajime Hirao, [d,e] Hiromu Kusuda, [b] Susumu Kitagawa [a] and Easan Sivaniah [a] *

a. Institute for Integrated Cell-Material Sciences (iCeMS), Kyoto University, 606-8501 Kyoto, Japan.

b. Department of Energy Science and Technology, Kyoto University, Kyoto, Japan.

c. Department of Chemical Engineering, Imperial College, London, SW7 2AZ, UK.

d. Department of Biology and Chemistry, City University of Hong Kong, Tat Chee Avenue, Kowloon, Hong Kong, China

e. Division of Chemistry and Biological Chemistry, School of Physical and Mathematical Sciences, Nanyang Technological University, 21 Nanyang Link, Singapore 637371

*Correspondence and requests for materials should be addressed to E.S. Email: esivaniah@icems.kyoto-u.ac.jp

© 2017 Macmillan Publishers Limited, part of Springer Nature. All rights reserved.

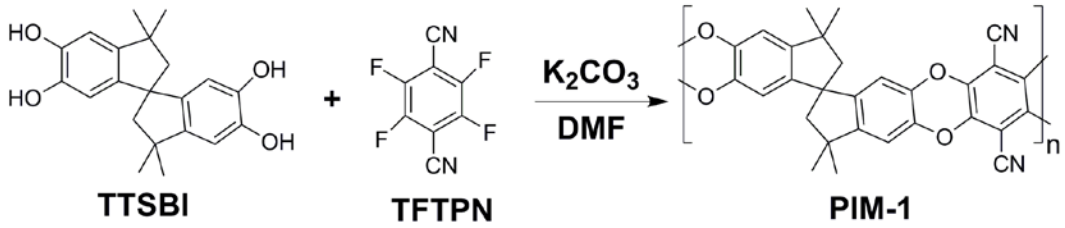

Supplementary Figure 1: Synthesis of PIM-1.
TTSBI: 5,5′,6,6′-tetrahydroxy-3,3,3′,3′ tetramethylspirobisindane; TTFPN: 2,3,5,6-tetrafluoroterephthalonitrile; Solvent was dimethylformamide.

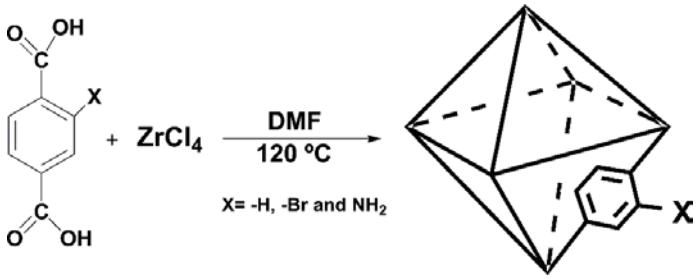

Supplementary Figure 2: UiO-66 synthesis. Reaction mechanism and chemical formula of UiO-66 MOFs.

© 2017 Macmillan Publishers Limited, part of Springer Nature. All rights reserved.

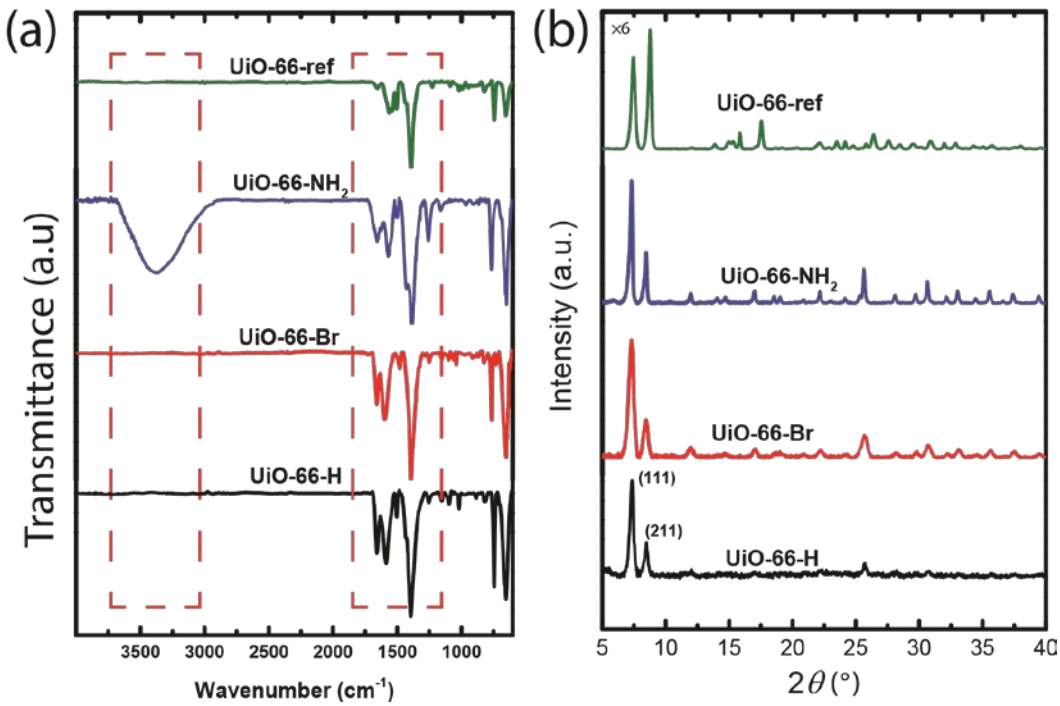

Supplementary Figure 3: FTIR and PXRD of UiO-66 particles.
(a) FTIR spectra, (b) PXRD patterns of Zr-MOFs particles: UiO-66-H, UiO-66-Br, UiO-66-NH_2 and UiO-66-ref. The FTIR spectra of the water modulated functionalized (-Br and -NH_2) UiO-66 particles are compared with the spectra of the parent water modulated UiO-66-H particles. All the structures showed a peak at 1550–1650 cm^{-1} corresponding to the symmetric stretching of carboxylate groups (υ(COO)), which is coordinated with metal centers during the deprotonation. Weak peak in the region of 1450–1500 cm^{-1} belongs to the stretching vibration of C-C in the aromatic compound of organic linker ring. The strong peak centered around 1400 cm^{-1} was ascribed to symmetric stretching of C–O bonds in the carboxylic acid groups. The FTIR spectrum for UiO-66-Br showed similar features to the one obtained for UiO-66-H particles. Although there is no specific carbon-halogen stretching vibration modes for aromatic halogen structures, the changes in the peak intensities which are sensitive to the bromo-functionality (e.g. at 680 cm^{-1}) are observed in the FTIR spectrum. Compared with the FTIR spectrum of UiO-66, the stretching vibration adsorption of the amine groups in UiO-66-NH_2 are clearly observed in high frequency region at 3000-3500 cm^{-1}. A peak at lower frequencies centred at 1250 cm^{-1} corresponds to the N–H bending vibration and the characteristic C–N stretching of aromatic amines. The PXRD pattern of pristine UiO-66 showed two peaks at 7.5° and 8.5° corresponding to [111] and [200] crystal planes, respectively and concur well with existing literature. The PXRD patterns of water modulated synthesized MOFs showed similar features, indicating an isostructural UiO-66 framework topology.

© 2017 Macmillan Publishers Limited, part of Springer Nature. All rights reserved.

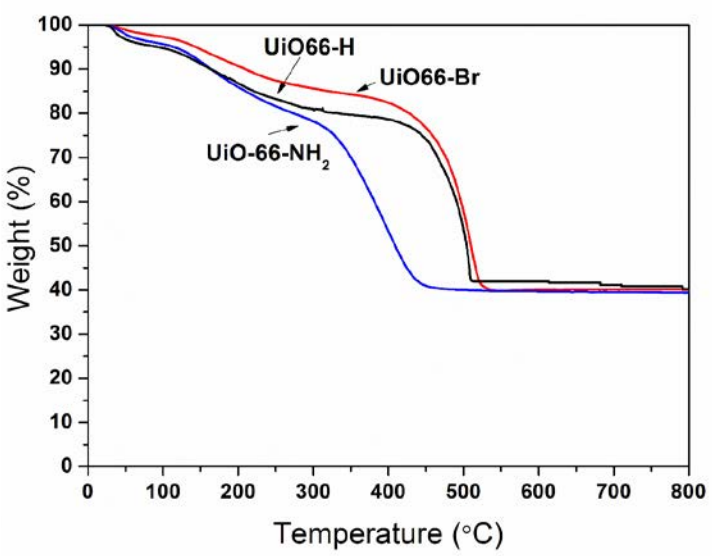

Supplementary Figure 4: TGA of water modulated Zr-MOFs particles.
TGAs of nanoparticles exhibited around 5% weight loss at around 75-100°C, corresponds to the departure of the guest molecules (chloroform and/or H_2O) followed by a drop at around 200°C which is due to the dehydration of the $Zr_6O_4(OH)_4$ nodes to Zr_6O_6. The final step near 350-500°C is attributed to decomposition of the organic linkers. In the case of MMMs, thermal degradation of PIM-1 started at around 390˚C. Above this temperature, continuous weight loss was observed. The thermal stabilities are improved upon the introduction of UiO-66-NH_2 nanoparticles into the PIM-1 matrix and the slope of weight reduction decreases as the amount of particles in the polymer increase. As the temperature increased above 400 °C the MMMs showed a slightly enhanced decomposition temperatures (Td) depending on the UiO-66 loadings.

© 2017 Macmillan Publishers Limited, part of Springer Nature. All rights reserved.

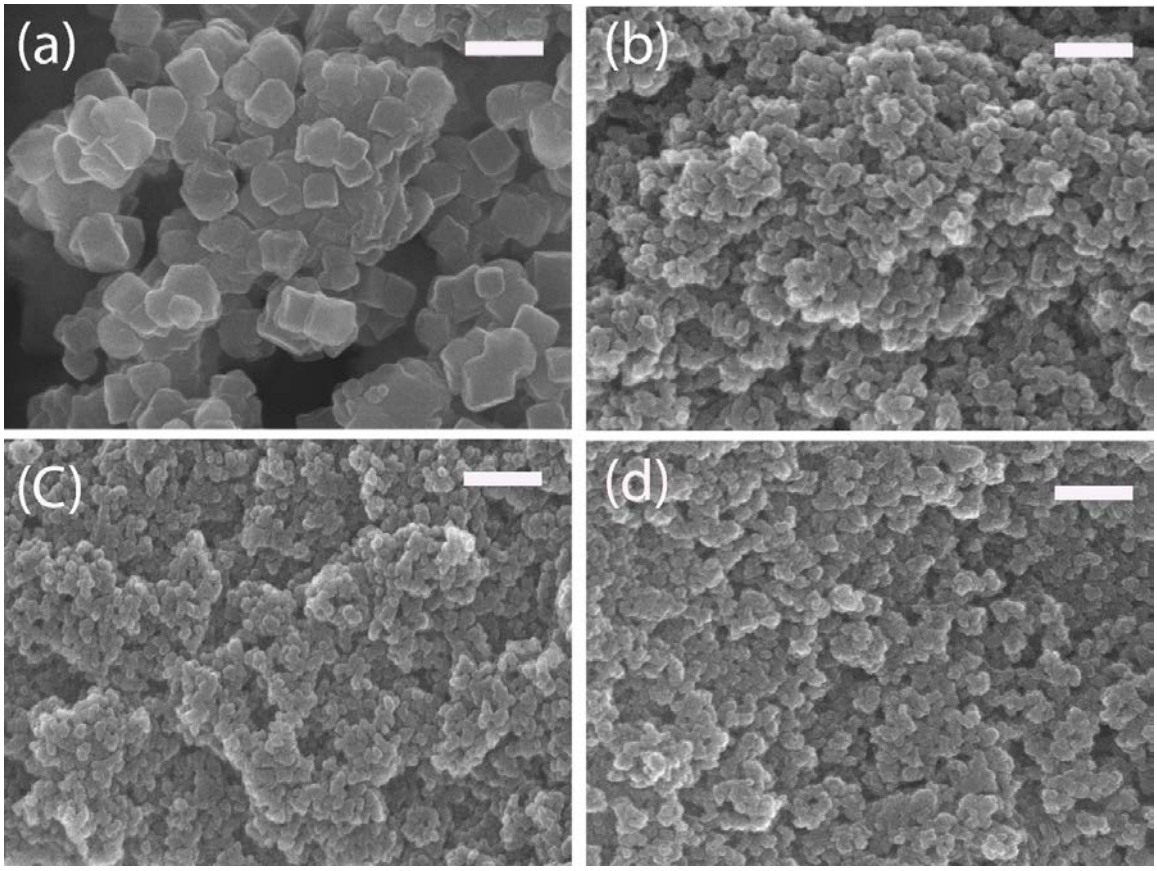

Supplementary Figure 5: SEM images of UiO-66 particles.
(a) UiO-66-ref particles, (b) water modulated UiO-66-H nanoparticles, (c) water modulated UiO-66-Br nanoparticles and (d) water modulated UiO-66-NH_2 nanoparticles (scale bars: 200 nm).

© 2017 Macmillan Publishers Limited, part of Springer Nature. All rights reserved.

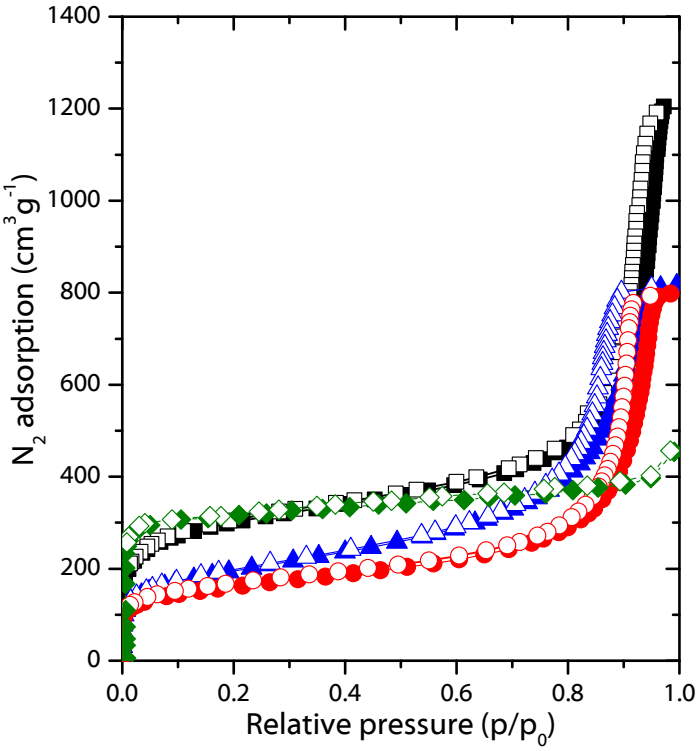

Supplementary Figure 6: Nitrogen adsorption studies (at 77K) of UiO-66 particles.
(Green diamond) UiO-66-ref, (black square) UiO-66-H, (blue triangle) UiO-66-NH_2, (red circle) UiO-66-Br particles. Open and closed markers represent adsorption and desorption data, respectively (P_0=1 atm). N_2 sorption isotherms measured at 77 K were used to evaluate the surface area, crystal structure and porosity of the UiO-66 MOFs (Supplementary Figure 6). Almost all modulated MOFs exhibited hybrid type I/IV isotherms with hysteresis between adsorption and desorption isotherms while Type I isotherms are indicative of microporous structure (pore size less than 2 nm) observed for non-modulated UiO-66-ref. Type IV isotherms are strong evidence of mesoporous structure (pore size between 2 and 50 nm) which may come from the interstitial voids between the nanoparticles of modulated synthesized particles [4].

© 2017 Macmillan Publishers Limited, part of Springer Nature. All rights reserved.

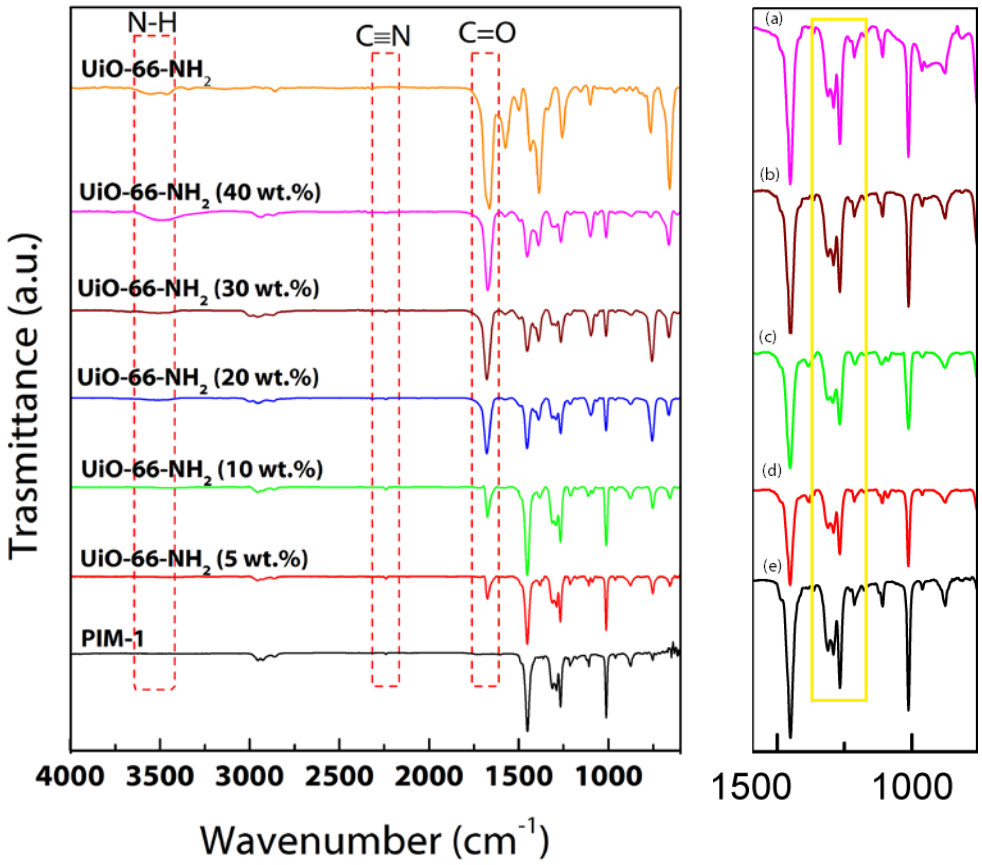

Supplementary Figure 7: ATR-FTIR spectra of the pure PIM-1 and PIM-1/UiO-66-NH_2 MMMs. In right side graph (a) UiO-66-ref (10 wt.%), (b) UiO-66-ref (5 wt. %), (c) UiO-66-NH_2 (10 wt.%), (d) UiO-66-NH_2 (5 wt.%) and (e) PIM-1. The ATR-FTIR of pure PIM-1 match existing literature in the material well [7] including C-H stretching within the methyl (C-CH_3) groups and methylene (CH_2) groups at around 2950, 2930 and 2840 cm^{-1}, C-H bending vibrations within methyl and methylene groups (1455 cm^{-1}), nitrile groups (-CN) at 2238 cm^{-1}, aromatic bending (C=C) at 1607 cm^{-1}, C-O stretching over 1300-1000 cm^{-1}. In the spectrum of MMM made by UiO-66-NH_2 the appearance of the broad N-H band at 3200-3600 cm^{-1} as well as the C=O band at 1650-1710 cm^{-1} indicate the presence of MOF particles inside the PIM-1 matrix. Also, there is a decrease in absorption between 1300 and 1100 cm^{-1} in these samples. This could be due to hydrogen bonding between the aromatic ether groups of the PIM-1 and the amine group grafted to the UiO-66 external surface[8]. The comparison FTIR data showed that the intensity of the signals related to ether group stretching, 1300-1100 cm^{-1}, significantly decreased in modulated-functionalized UiO-66-NH_2 MMMs (5 and 10 wt. % loading) while it was almost constant for MMMs including UiO-66-ref particles.

© 2017 Macmillan Publishers Limited, part of Springer Nature. All rights reserved.

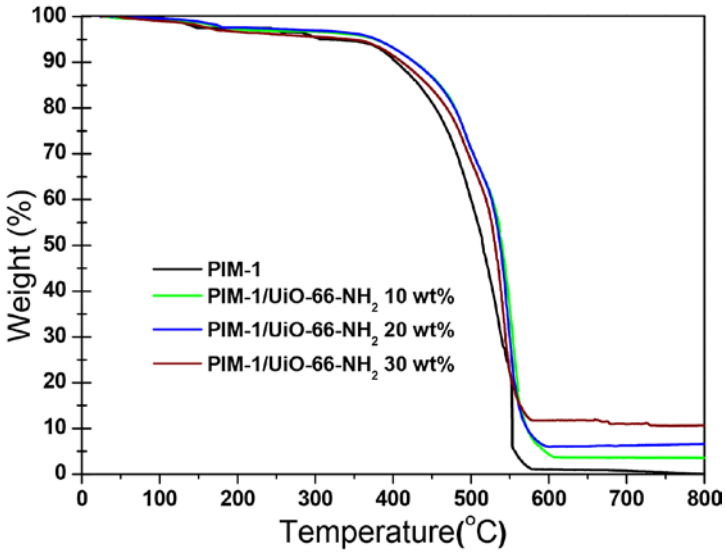

Supplementary Figure 8: TGA of the pure PIM-1 and PIM-1/UiO-66-NH_2 MMMs.
Thermal degradation of PIM-1 started at around 390˚C. Above this temperature, continuous weight loss was observed. The thermal stabilities are improved upon the introduction of UiO-66-NH_2 nanoparticles into the PIM-1 matrix and the slope of weight reduction decreases as the amount of particles in the polymer increase. As the temperature increased above 400 °C the MMMs showed a slightly enhanced decomposition temperatures (Td) depending on the UiO-66 loadings.

© 2017 Macmillan Publishers Limited, part of Springer Nature. All rights reserved.

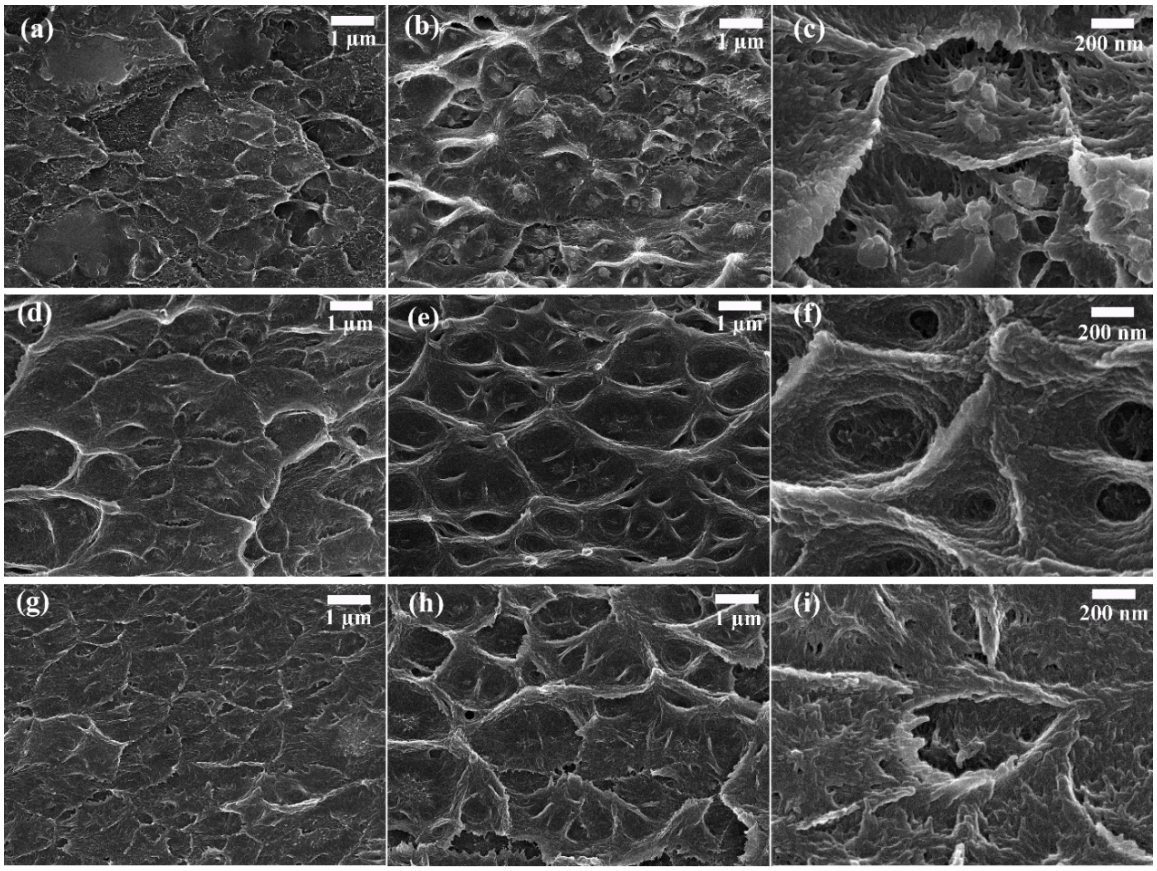

Supplementary Figure 9: SEM images of cross-sections of PIM-1/UiO-66 MMM.
(a) 5 wt.% UiO-66-ref, (b) 20 wt.% UiO-66-ref, (c) 20 wt.% UiO-66-ref, (d) 5 wt.% water modulated UiO-66-H, (e) 20 wt.% water modulated UiO-66-H, (f) 20 wt.% water modulated UiO-66-H (high magnification), (g) 5 wt.% water modulated UiO-66-NH_2, (h) 20 wt.% water modulated UiO-66-NH_2 and (i) 20 wt.% water modulated UiO-66 (high magnification).

© 2017 Macmillan Publishers Limited, part of Springer Nature. All rights reserved.

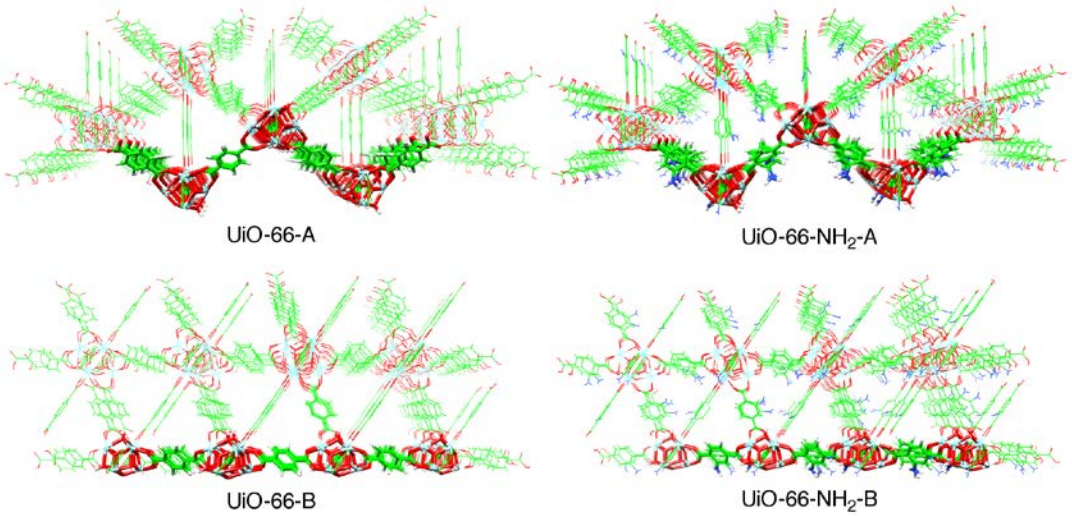

Supplementry Figure 10: Models of the UiO-66 and UiO-66-NH_2 frameworks.
UiO-66-A and UiO-66-NH_2-A feature corrugated surfaces, while UiO-66-B and UiO-66-NH_2-B have flat surfaces. Target atoms at which PIM-1 configurations were sampled are shown in stick representation.

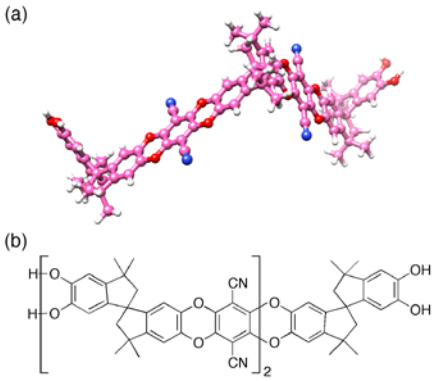

Supplementary Figure 11: PIM-1 chemical structure.
(a) Optimized structure of the PIM-1 model. (b) Chemical structure of the PIM-1 model.

© 2017 Macmillan Publishers Limited, part of Springer Nature. All rights reserved.

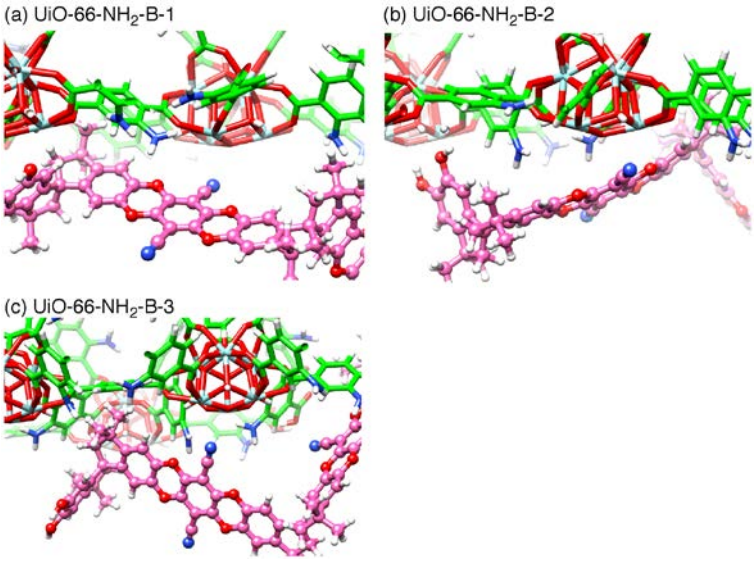

Supplementary Figure 12. The first (a), second (b), and third (c) most stable structures of the UiO-66-NH_2-B/PIM-1 composite. The MOF and PIM-1 are shown in stick and ball-and-stick representations, respectively.

© 2017 Macmillan Publishers Limited, part of Springer Nature. All rights reserved.

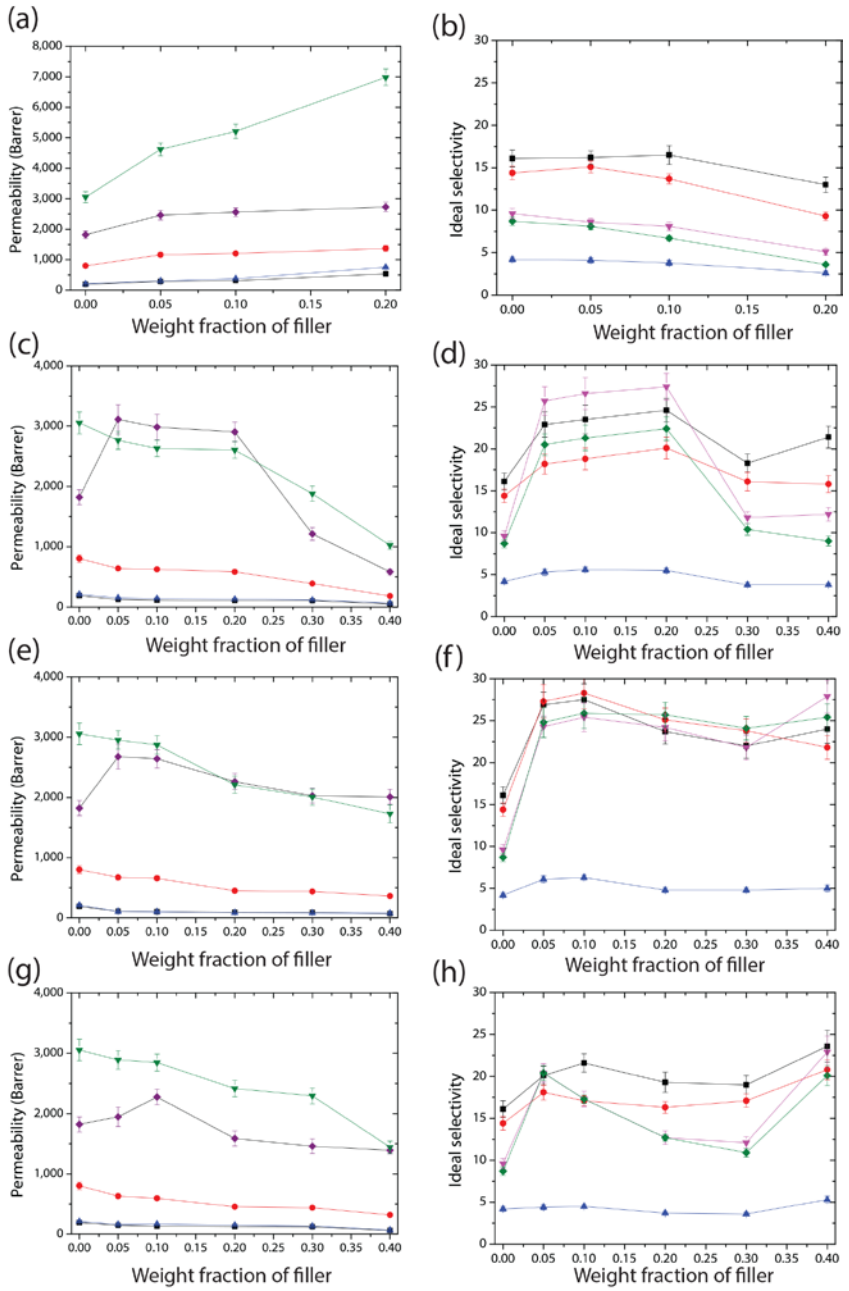

Supplementary Figure 13: Permeability and ideal selectivity of PIM-1/UiO-66 MMMs at 4 bar and 25 ˚C. (a), (b) UiO-66-ref, (c), (d) UiO-66-H, (e), (f) UiO-66-NH_2 and (g), (h) UiO-66-Br (green triangle): CO_2, (purple diamond): H_2, (red circle): O_2 (blue triangle): CH_4 and (black square): N_2 in permeability graphs and (brown triangle): H_2/N_2, (green diamond): H_2/CH_4, (red circle): CO_2/CH_4, (blue triangle): O_2/N_2 and (black square): CO_2/N_2 in selectivity graphs. As we have plotted Supplementary Figure 13, an initial increase of H_2 permeability is consistently seen for all additions of MOF filler, nanosized or not, functionalized or not. This is then seen to decrease as the aggregated modulated filler loading increases. By comparison, the permeability of all other gases decreases monotonically upon addition of the modulated fillers and increase on addition of the non-modulated filler. This observation of anomolous H_2 permeation in mixed matrix systems is sometime noted e.g. by Budd and co-workers for PIM-1 MOF composites (Separation and Purification Technology 173 (2017): 304-313) or by Basu et al. in a study of in polyimide/Cu_3(BTC) MMMs (Journal of membrane science 362 (1), 478-487). One speculative cause is that the modulated fillers have not completely eliminated the effects of microvoids, at least at the level of the kinetic diameter of H_2, which at 2.8Å, is smaller than the remaining cluster of gases (3.3-3.7Å) tested in this study. Over time such defects would be expected to relax, so that the findings of high hydrogen selectivity over other gas pairs is likely a transient effect. However, such a speculation would require a further focused study for verification.

© 2017 Macmillan Publishers Limited, part of Springer Nature. All rights reserved.

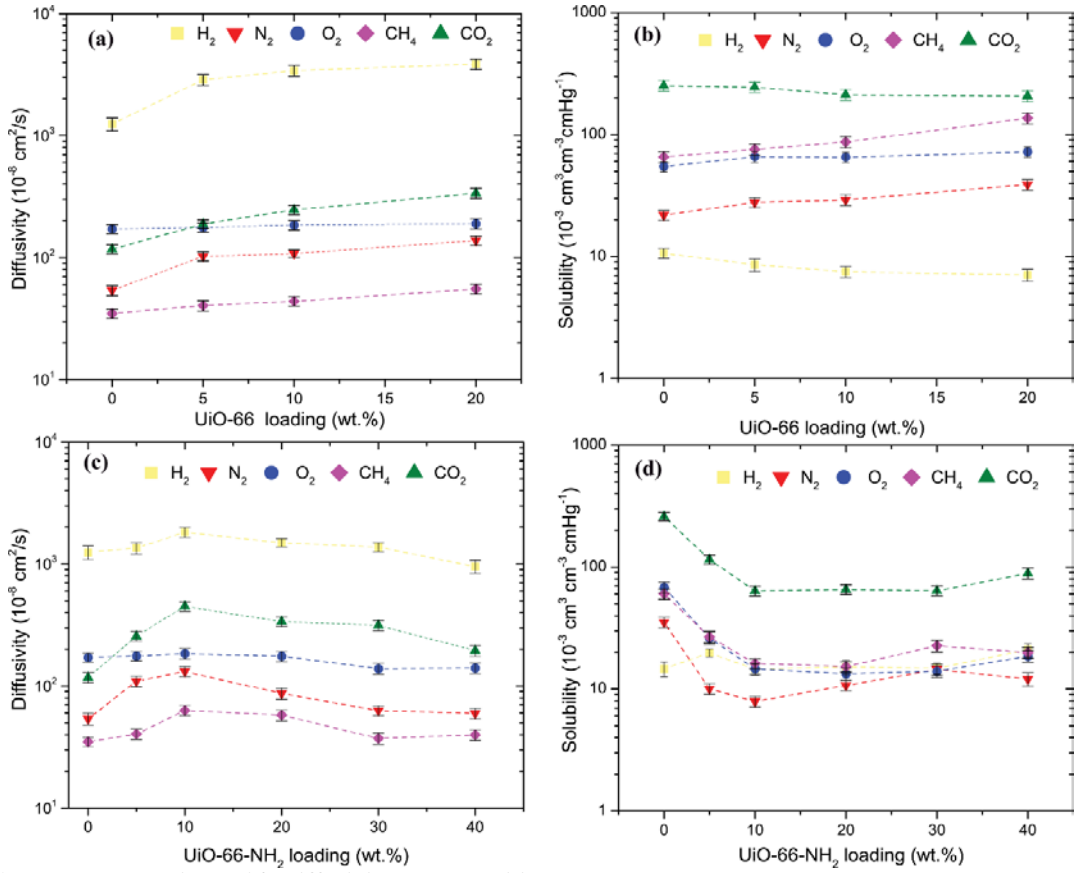

Supplementary Figure 14. Diffusivity and solubility.
(a) Diffusion coefficients and (b) solubility of gases in PIM-1/UiO-66-ref, (c) diffusion coefficients and (d) solubility of gases in PIM-1/ water modulated UiO-66 –NH_2 at 4 bar and 25 ˚C.

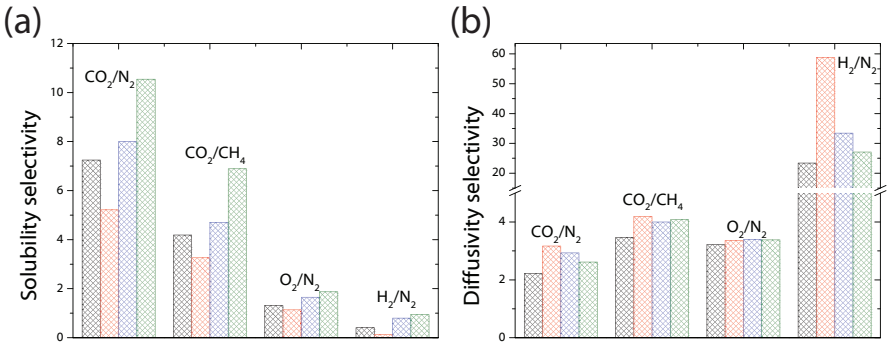

Supplementary Figure 15. (a) Solubility and (b) diffusivity selectivity of various gas-pairs in Zr-MOF based MMMs (black: pure PIM-1, red: 10 wt.% UiO-66-ref, blue: 10wt.% UiO-66-H and green: 10wt.% UiO-66-NH_2 MMMs).

© 2017 Macmillan Publishers Limited, part of Springer Nature. All rights reserved.

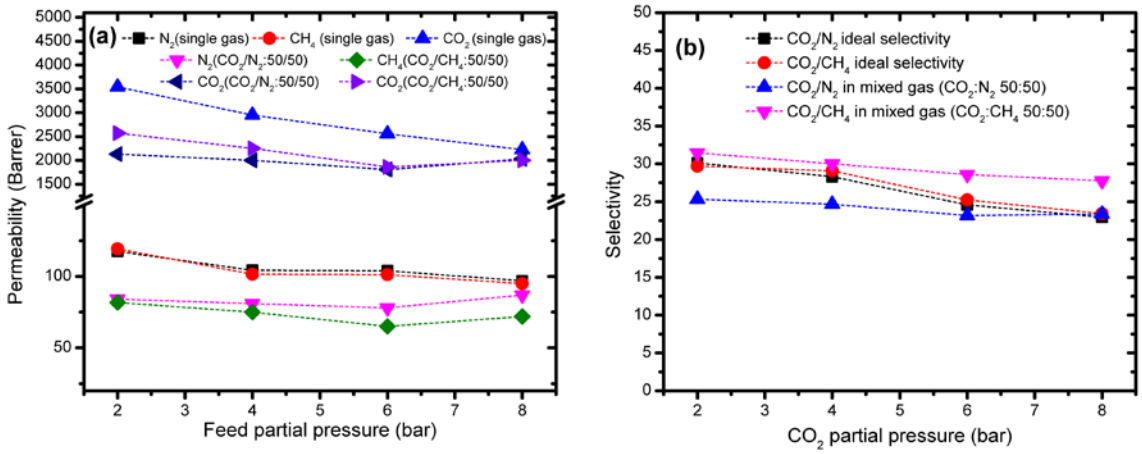

Supplementary Figure 16. (a) Single and mixed gas permeability versus feed gas partial pressure in MMMs containing 10 wt.% modulated UiO-66-NH_2. (b) Selectivity versus CO_2 partial pressure in MMMs containing 10 wt.% modulated UiO-66-NH_2. The mixed gas separation performance was measured with total feed pressure up to 16 bar using mixed gases with 50 vol.% of CO_2.

© 2017 Macmillan Publishers Limited, part of Springer Nature. All rights reserved.

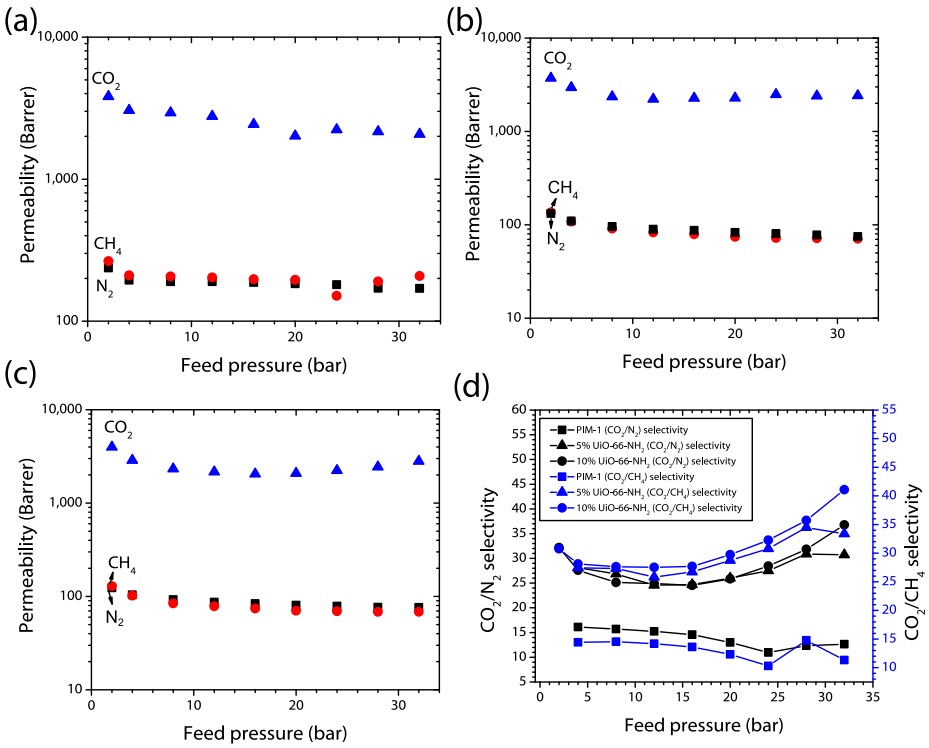

Supplementary Figure 17: Effect of pressure on gas permeation properties of PIM-1 and UiO-66-NH_2 MMMs at 25 °C. Permeability vs. feed pressure in (a) PIM-1, (b) PIM-1/UiO-66-NH_2 (5 wt.%), (c) PIM-1/UiO-66-NH_2 (10 wt.%) and (d) CO_2/N_2 and CO_2/CH_4 selectivity *vs.* feed pressure in PIM-1, 5 and 10 wt.% PIM-1/UiO-66-NH_2. The gas permeability of typical glassy polymers declines with increasing pressure due to the filling the sorption sites, while at the elevated pressures, gas permeability approaches a constant value[9]. However, for more strongly interacting penetrants like CO_2, glassy polymers show an upward-increasing permeability due to plasticization at high pressures[10]. Therefore, the typical plasticization of glassy polymer membrane was observed by initial decrease in permeability with pressure at low pressures followed by a continuous increasing in CO_2 permeability with increasing pressure. In contrast with the conventional glassy polymers, microporous polymers like PIM-1 doesn't plasticize by CO_2 and show a decrease in permeability with increasing of CO_2 feed pressure in wide range of pressure. This phenomena might be related to the break down in microporous structure of PIM-1 and decrease in high initial free volume of the polymer [10]. Composite membranes comprising 5 and 10 wt.% UiO-66-NH_2 particles showed similar behavior as PIM-1. However, the amount of reduction in CO_2 permeability in MMMs at high pressure was less than PIM-1.

© 2017 Macmillan Publishers Limited, part of Springer Nature. All rights reserved.

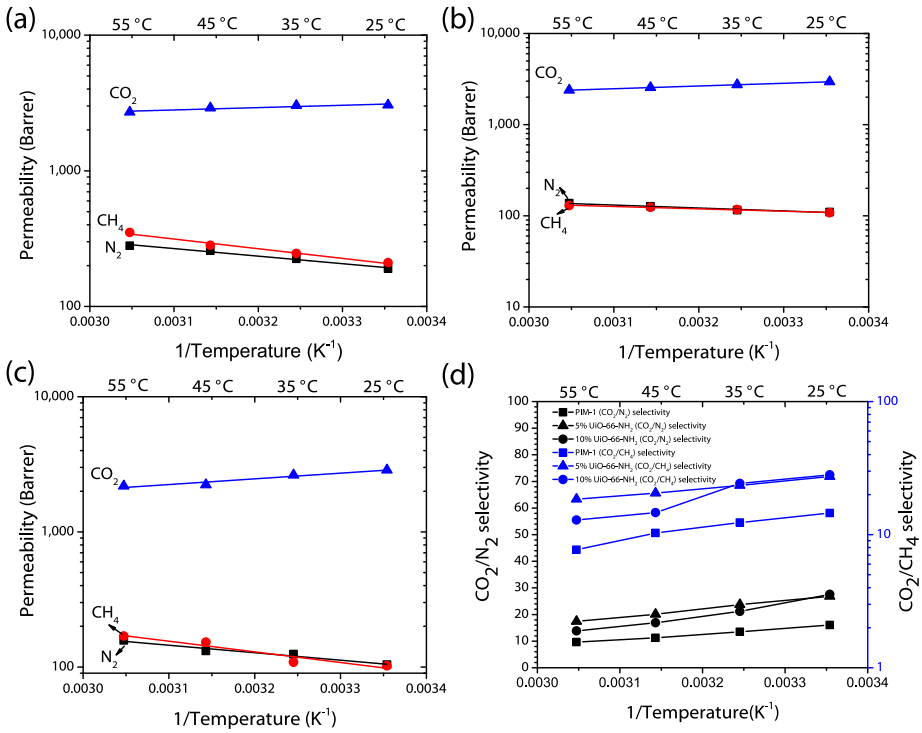

Supplementary Figure 18: Effect of temperature on gas permeation properties of PIM-1 and UiO-66-NH_2 MMMs at 4 bar. Permeability *vs.* reciprocal temperature (a) PIM-1, (b) PIM-1/UiO-66-NH_2 (5 wt.%), (c) PIM-1/UiO-66-NH_2 (10 wt.%) and (d) CO_2/N_2 and CO_2/CH_4 selectivity *vs.* reciprocal temperature in PIM-1, 5 and 10 wt.% PIM-1/UiO-66-NH_2. The temperature dependence of gas permeability in polymers is governed by the Arrhenius equation: $P = P_0 \exp(-E_p/RT)$

where P_0 is a pre-exponential factor (cm^3(STP).cm/cm^2.s.cm-Hg), E_p is the activation energy of permeation (J/mol), T is the experiment temperature (K) and R is the universal gas constant (8.314 J/mol.K). Ep values for PIM-1 and composite membranes were calculated from the slopes ($-E_p/R$) of the linear curve-fits through the permeation data and summarized in Supplementary Table 5. CH_4 and N_2 permeability of PIM-1 increased with increasing temperature whilst the CO_2 permeability decreased. The absolute activation energy values are significantly lower in CO_2 than CH_4 and N_2. Therefore, the CO_2 separation factors reduces by increasing temperature. Gas permeability of UiO-66-NH_2 MMMs showed almost similar trend as PIM-1 to the temperature changes with higher absolute amounts of E_p. This results suggest that the permeation properties of MMMs are more dependent on temperature than PIM-1. On the contrary, increasing temperature exhibits a decrease in permselectivity due to increases the free volume of the polymer and diminishing the sieving properties of the membranes[11].

© 2017 Macmillan Publishers Limited, part of Springer Nature. All rights reserved.

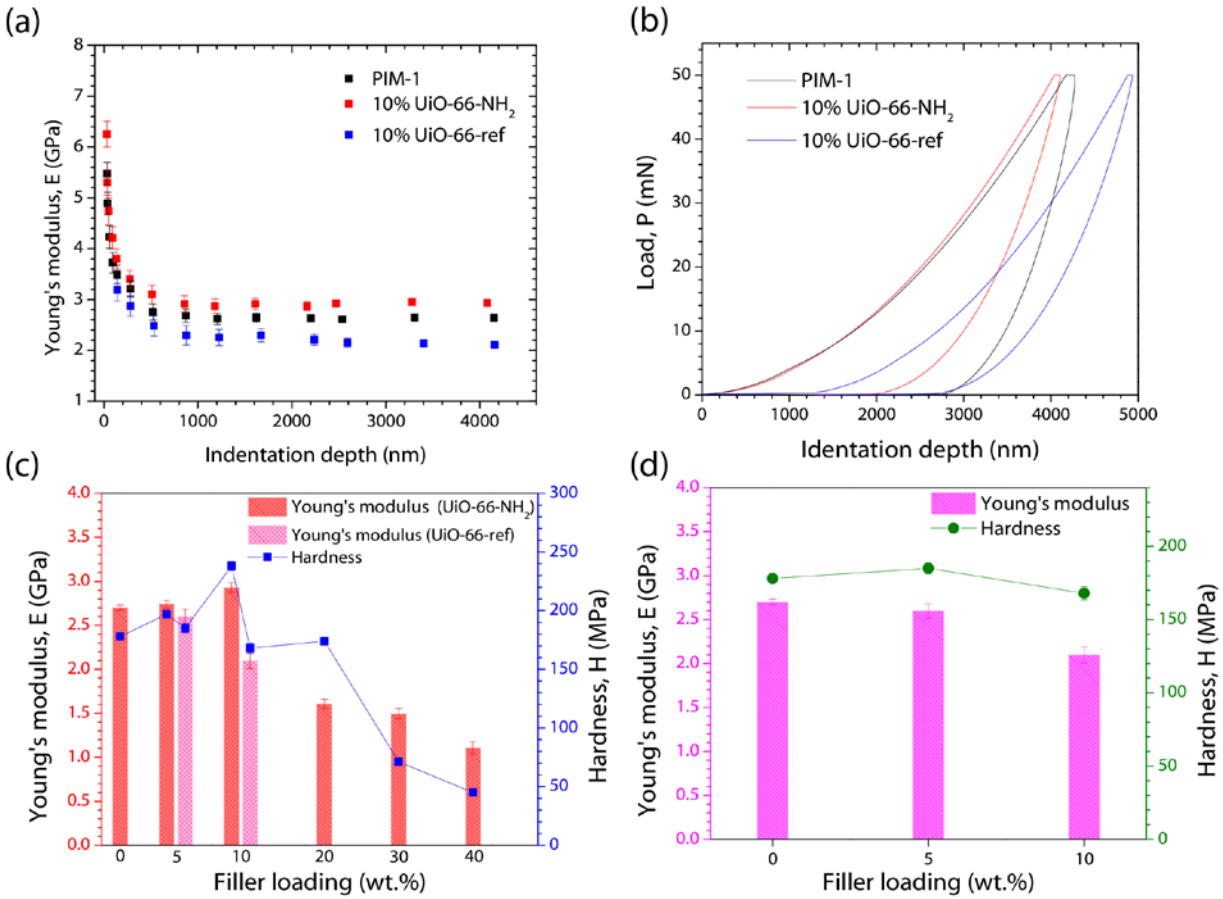

Supplementary Figure 19: Mechanical properties. (a) Young modulus of representative membranes as a function of indentation depth (30 nm to 4 μm), (b) Representative P-h curves for PIM-1 and composite membranes at different loading of UiO-66-NH_2 particles, (c) Young's modulus and indentation hardness of PIM-1/UiO-66-NH_2 MMMs at different loadings (depth of 4) and (d) Young's modulus and indentation hardness of PIM-1/UiO-66-ref MMMs at different loadings. Error bars represent the standard error of 20 indents. The measurements were performed at ambient temperature. The indenter axes were aligned normal to the membrane planes. The average values of the elastic modulus (E) and the hardness (H) were calculated in the depth of 4 μm.

© 2017 Macmillan Publishers Limited, part of Springer Nature. All rights reserved.

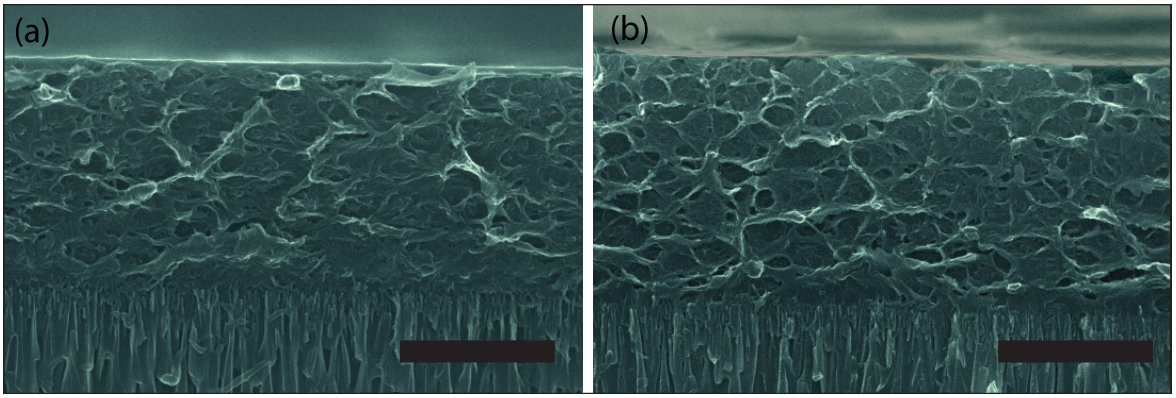

Supplementary Figure 20: Thin film membranes on the surface of ceramic support. (a) PIM-1 and (b) PIM-1/UiO-66-NH_2 (5wt.%). The scale bars are 500 nm.

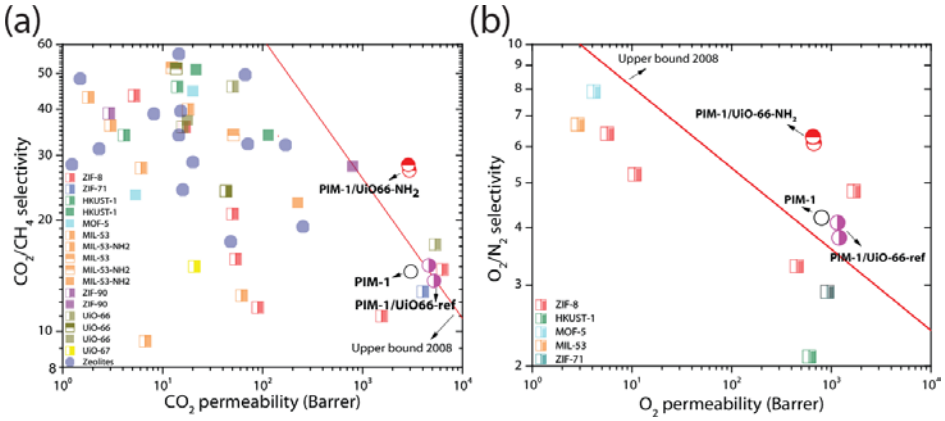

Supplementary Figure 21: Selectivity versus permeability plots for typical gas pairs (a) CO_2/CH_4 and (b) O_2/N_2. (◓,◓,◑) respectively refer to (5 and 10 wt.% filler loadings) MMMs with smaller functionalized UiO-66-NH_2, UiO-66-H fillers and larger un-functionalized UiO-66-ref fillers; (○) refers to pure PIM-1. Also shown is recently reviewed separation performance of various classes of MOF (⬒,◨,■; refer to enhancements to selectivity, permeability, or both, respectively) and zeolite (●) based mixed matrix membranes (see SI for full data set, Supplementary Tables 6-10).

© 2017 Macmillan Publishers Limited, part of Springer Nature. All rights reserved.

Supplementary Table 1: Specific surface area and pore volume and N_2 uptake of UiO-66s nanoparticles. It is generally admitted that the micropores are filled at very low relative pressures which are the result of overlapping of adsorption potentials of crystal pore walls [5]. Therefore, the significant lower amount of nitrogen sorption (at P/P_0= 0.1) in modulated particles (UiO-66-ref) might be in accordance with their lower crystallinity compare with non-modulated particles [6]. The data is in agreement with the PXRD of UiO-66 structures that show lower signal intensities in modulated particles than non-modulated one (please see PXRD of particles).

Zr-MOFs	BET surface area (m^2/g)	Langmuir Surface area (m^2/g)	Total pore volume (cm^3/g)	N_2 uptake ($cm^3\ g^{-1}$)
UiO-66-ref	1320.1	1478.2	0.43	300
UiO-66-H	1115.4	1187.9	0.41	270
UiO-66-NH_2	708.6	765.3	0.29	170
UiO-66-Br	585.4	639.4	0.25	145

[1.] Nitrogen uptakes are measured at relative pressure (P/P_0) of 0.1.

Supplementary Table 2. Adhesion energies (kcal/mol) for UiO-66-A and UiO-66-NH_2-A. Data for the top 3 configurations are shown.

UiO-66-A			
	Adhesion[a]	Deformation[b]	Rigid adhesion[c]
UiO-66-A-1	-55.3	8.9	-64.2
UiO-66-A-2	-51.7	4.4	-56.1
UiO-66-A-3	-48.9	6.0	-54.9
UiO-66-NH_2-A			
	Adhesion[a]	Deformation[b]	Rigid adhesion[c]
UiO-66-NH_2-A-1	-72.2	6.9	-79.1
UiO-66-NH_2-A-2	-59.9	4.3	-64.2
UiO-66-NH_2-A-3	-52.7	4.1	-56.8

[a] The energy released when the relaxed PIM-1 model is adsorbed on the MOF. This is the sum of the rigid adhesion energy and the deformation energy.
[b] The energy released when the adsorbed PIM-1 model is relaxed on the MOF.
[c] The energy released when the frozen PIM-1 model is adsorbed on the MOF.

Supplementary Table 3. Adhesion energies (kcal/mol) for UiO-66-B and UiO-66-NH_2-B. Data for the top 3 configurations are shown.

UiO-66-B			
	Adhesion[a]	Deformation[b]	Rigid adhesion[c]
UiO-66-B-1	-47.2	3.3	-50.5
UiO-66-B-2	-44.5	2.2	-46.7
UiO-66-B-3	-39.4	1.7	-41.1
UiO-66-NH_2-B			
	Adhesion[a]	Deformation[b]	Rigid adhesion[c]
UiO-66-NH_2-B-1	-47.1	7.3	-54.4
UiO-66-NH_2-B-2	-44.7	3.1	-47.8
UiO-66-NH_2-B-3	-44.4	2.8	-47.3

[a] The energy released when the relaxed PIM-1 model is adsorbed on the MOF. This is the sum of the rigid adhesion energy and the deformation energy.
[b] The energy released when the adsorbed PIM-1 model is relaxed on the MOF.
[c] The energy released when the fixed PIM-1 model is adsorbed on the MOF.

© 2017 Macmillan Publishers Limited, part of Springer Nature. All rights reserved.

Supplementary Table 4. Pure gas permeation properties of PIM-1 and PIM-1/Zr-MOFs mixed matrix membranes with different functionalities and filler loadings at 4 bar and 298 K. Permeation data calculated based on the average of three measurements, errors represent the standard errors.

Loading of Zr-MOFs	Permeability (Barrer)					Selectivity				
	H_2	N_2	O_2	CH_4	CO_2	CO_2/N_2	CO_2/CH_4	O_2/N_2	H_2/N_2	H_2/CH_4
UiO-66-ref										
0 (PIM-1)	1820±124	190±12	802±65	210±12	3054±180	16.1±1	14.5±0.8	4.2±0.3	9.6±0.6	8.7±0.5
5 wt.%	2461±154	285±14	1162±77	305±15	4620±210	16.2±0.8	15.1±0.7	4.1±0.2	8.6±0.4	8.1±0.4
10 wt.%	2560±146	315±21	1205±68	381±16	5210±233	16.5±1.1	13.7±0.6	3.8±0.3	8.1±0.5	6.7±0.3
20 wt.%	2730±158	536±38	1370±89	754±40	6981±275	13.0±0.9	9.3±0.5	2.6±0.2	5.1±0.4	3.6±0.2
UiO-66-H										
5 wt.%	3112±243	121±8	639±32	152±10	2765±148	22.9±1.5	18.2±1.2	5.3±0.4	25.7±1.7	20.5±1.3
10 wt.%	2985±211	112±8	626±30	140±10	2631±136	23.5±1.7	18.8±1.3	5.6±0.3	26.6±1.9	21.3±1.5
20 wt.%	2905±164	106±6	582±25	129±8	2606±140	24.6±1.4	20.1±1.3	5.5±0.3	27.4±1.6	22.4±1.4
30 wt.%	1213±108	103±6	388±21	117±8	1880±126	18.3±1.1	16.1±1.1	3.8±0.2	11.8±0.7	10.4±0.7
40 wt.%	583±46	48±3	183±12	65±4	1023±65	21.4±1.3	15.8±1	3.8±0.2	12.2±0.8	9.0±0.6
UiO-66-NH_2										
5 wt.%	2676±206	110±6	671±36	108±8	2952±152	26.9±1.5	27.3±2	6.1±0.3	24.3±1.3	24.8±1.8
10 wt.%	2641±152	104±7	658±38	102±8	2869±155	27.5±1.9	28.3±1.9	6.3±0.4	25.4±1.7	25.9±1.8
20 wt.%	2262±135	93±6	449±28	88±5	2210±141	23.7±1.5	25.1±1.4	4.8±0.3	24.2±1.6	25.7±1.5
30 wt.%	2028±124	91±6	438±25	84±5	2005±135	22.0±1.5	23.8±1.4	4.8±0.3	21.8±1.5	24.1±1.4
40 wt.%	2009±125	72±6	362±18	79±6	1727±148	24.0±1.7	21.8±1.4	5.0±0.4	27.9±1.9	25.4±1.6
UiO-66-Br										
5 wt.%	2946±161	144±8	630±37	160±8	2890±155	20.1±1.1	18.1±0.9	4.4±0.3	20.4±1.1	18.4±0.9
10 wt.%	2275±143	132±7	595±32	166±6	2846±141	21.6±1.1	17.1±0.6	4.5±0.2	17.3±0.9	13.7±0.5
20 wt.%	1587±110	125±8	455±30	148±6	2416±136	19.3±1.2	16.3±0.7	3.7±0.2	12.7±0.8	10.7±0.4
30 wt.%	1459±95	121±7	438±30	134±6	2294±128	19.0±1.1	17.1±0.8	3.6±0.2	12.1±0.7	10.9±0.5
40 wt.%	1391±106	61±5	319±16	69±4	1441±102	23.6±1.9	20.8±1.2	5.3±0.4	22.9±1.9	20.1±1.2

Supplementary Table 5: Activation energy of permeation (Ep) for PIM-1 and PIM-1/UiO-66-NH_2 MMMs.

Gas	Ep (J/mol)		
	PIM-1	5 wt.% UiO-66-NH_2	10 wt.% UiO-66-NH_2
N_2	4,626	2,683	4,601
CH_4	5,927	2,154	6,551
CO_2	-1,432	-2,482	-3,499

© 2017 Macmillan Publishers Limited, part of Springer Nature. All rights reserved.

Supplementary Table 6: Overview of representative MOF based membranes for CO_2/N_2 separation.

Membrane		Operation conditions			Separation performance		Ref.
MOFs	**Polymers**	**Feed gas composition (CO_2 vol.%)**	**Pressure (bar)**	**Temperature (°C)**	**CO_2 permeability (Barrer)**	**CO_2/N_2 selectivity**	
ZIF-8	Matrimid	Pure	2.7	25	4.7	26.2	18
	PPEEs	Pure	1	30	50	24.5	19
	Matrimid	Pure	4	22	16.6	19	20
	6FDA-DAM:DABA (4:1)	Pure	1.4	30	553	19.3	21
	PIM-1	Pure	1	20-22	6300	18	12
	6FDA-durene	Pure	3.5	35	1552.9	11.3	22
	PBI-BuI	Pure	20	35	5.2	16	23
ZIF-7	Pebax	Pure	2.75	20	111	30	24
HKUST-1	PDMS	Pure	-	-	3050	8.9	25
	PMDA-ODA	Pure	10	25	227.2	5.5	26
	PPO	Pure	-	30	115	26	27
	Ultem	Pure	3.5	35	4.1	28	28
MOF-5	Matrimid	Pure	2	35	20.2	38.8	29
	PEI	Pure	6	25	5.4	28.4	30
MIL-53							
	Matrimid	Pure	2	35	51	28.3	31
Cu 1,4-BDC	PVAc	Pure	4.5	35	3.3	35.4	32
CPO-27	XLPEO	Pure	2	25	250	25	33
	6FDA-TMPDA	Pure	2	25	850	23	
	PDMS	Pure	2	25	2100	12	
UiO-66-NH_2	PSF	Pure	3	35	43	26	34
UiO-66	PIM-1	Pure	1	25	5340	21.36	35
ZIF-71	6FDA-durene	Pure	2	35	4006	12.9	36

© 2017 Macmillan Publishers Limited, part of Springer Nature. All rights reserved.

Supplementary Table 7: Overview of representative MOF based membranes for CO_2/CH_4 separation.

Membrane		Operation conditions			Separation performance		Ref.
MOFs	**Polymers**	**Feed gas composition (CO_2 vol.%)**	**Pressure (bar)**	**Temperature (°C)**	**CO_2 permeability (Barrer)**	**CO_2/CH_4 selectivity**	
ZIF-8	Matrimid	Pure	2.7	25	4.7	124.9	18
	PPEEs	Pure	1	30	50	20.8	19
	Matrimid	Pure	4	22	16.6	35.8	20
	Pebax	Pure	6.5	20	111	30	24
	PIM-1	Pure	1	20-22	6300	14.7	12
	6FDA-durene	Pure	3.5	35	1552.9	11	22
	PBI-BuI	Pure	20	35	5.2	43.6	23
	DM PBI-BuI	Pure	20	35	53.9	15.7	
	DBz PBI-BuI	Pure	20	35	89.8	11.6	
ZIF-7	Pebax	Pure	6.5	20	111	30	24
ZIF-71	6FDA-durene	Pure	2	35	4006	12.8	36
HKUST-1							
	PMDA-ODA	Pure	10	25	227.2	7	26
	6FDA-ODA	Pure	10	35	21.8	51.2	8
	PPO	Pure	-	30	115	34	27
	Ultem	Pure	3.5	35	4.1	34	28
	Matrimid	Mixed gas (50)	10	25	14	46	37
	PDMS	Pure	-	-	2900	3.6	25
MOF-5	Matrimid	Pure	2	35	20.2	44.7	29
	PMDA-ODA	Pure	6	25	0.27	56.8	38
	PEI	Pure	6	25	5.4	23.4	38
MIL-53							
	Matrimid	Pure	10	35	6.7	9.4	39
	Ultem	Pure	10	35	1.8	43.1	
	6FDA-ODA:DAM	Pure	10	35	61.5	12.5	
	PMP	Pure	3	35	12.4	51.8	40
	Matrimid	Pure	5	25	18	40	37
	PSF	Pure	3	35	6.1	27.7	41
MIL-53-NH2	Matrimid	Pure	3	25	9.2	2.1	39
	Ultem	Pure	3	25	3	36.2	
	6FDA-ODA:DAM	Pure	3	25	51.2	34.1	
	PMP	Pure	4	30	226	22.3	40
	PSF	Mixed gas(50)	10	35	2.4	117	42
ZIF-90	Ultem	Pure	4.5	35	2.9	39	43
	Matrimid	Pure	4.5	35	10.5	35	
	6FDA-DAM	Pure	2	35	800	28	
UiO-66	6FDA-ODA	Pure	10	35	50.4	46.1	8
	6FDA-ODA	Mixed gas (50)	10	35	50.4	42.3	
	PI	Mixed gas (50)	9	35	15.7	35.8	16
	PIM-1	Pure	1	25	5340	17.2	35
UiO-66-NH2	6FDA-ODA	Pure	10	35	13.7	51.6	8
	6FDA-ODA	Mixed gas (50)	10	35	13.7	44.7	
	PI	Mixed gas (50)	9	35	17.8	37.3	16
	PSF	Pure	3	35	43	24	34
UiO-67	6FDA-ODA	Pure	10	35	20.8	15	8
	6FDA-ODA	Mixed gas (50)	10	35	20.8	15	
Cu 1,4-BDC	PVAc	Pure	4.5	35	3.26	40.4	32

© 2017 Macmillan Publishers Limited, part of Springer Nature. All rights reserved.

Supplementary Table 8: Overview of representative zeolite based mixed matrix membranes for CO_2 separation.

Polymer/Filler	CO_2 permeability (Barrer)	CO_2/CH_4 selectivity	CO_2/N_2 selectivity	Ref.
Matrimid/Meso-ZSM-5	14.61	56.48	47.12	44
6FDA-DABA/ZSM-2	15.96	24.18	13.3	45
PES/Zeolite 4A	2.32	31.22	25.4	46
PPZ/SAPO	48	17.5	53	47
6FDA-DABA/APTES-LTL	20.1	28.74	-	48
PES/Zeolite NaN	1.24	28.33	-	49
PES/Zeolite AgA	1.5	48.39	-	
PEI/Silicalite-1	14.6	34	-	50
Matrimid/NaY	15.19	39.5	-	51
Pebax 1074/SAPO-34	170	32	75	52
PDMC/SSZ-13	67	49.6	-	53
Pebax 1657/Zeolite 4A	71.4	32.2	52.8	54

Supplementary Table 9: Pure polymer gas separation performance for CO_2/N_2 separation.

Polymer	CO_2 permeability (Barrer)	CO_2/N_2 selectivity	Ref.
Matrimid	9.52	30.7	18
PPEEs	5.72	30.1	19
Matrimid	8.07	22.4	20
6FDA-DAM:DABA (4:1)	200	20	21
PIM-1	4390	24.83	12
6FDA-durene	468.5	13.42	22
PBI-BuI	2.2	25	23
Pebax	3	25	24
PDMS	2500	8.5	25
PPO	70	15	27
Ultem	1.14	36.77	28
Matrimid	9	36	29
PEI	1.68	16.8	30
Matrimid	8.4	33.6	31
PVAc	2.44	32.1	32
XLPEO	380	22	33
6FDA-TMPDA	650	14	
PDMS	3100	9.5	
PSF	5.6	29.5	34
PIM-1	3620	20.1	35
6FDA-durene	959	14.7	36

© 2017 Macmillan Publishers Limited, part of Springer Nature. All rights reserved.

Supplementary Table 10: Pure polymer gas separation performance for CO_2/CH_4 separation.

Polymer	CO_2 permeability (Barrer)	CO_2/CH_4 selectivity	Ref.
Matrimid	9.52	39.5	18
PPEEs	5.72	22.9	19
Matrimid	8.07	35.2	20
PIM-1	4390	14.2	12
6FDA-durene	468.5	15.6	22
PBI-BuI	2.2	55	23
DM PBI-BuI	3	55	
DBz PBI-BuI	22	80	
Pebax	72	14	24
6FDA-durene	959	16.4	36
PMDA-ODA	14.4	44.1	26
PPO	70	15	27
Ultem	1.14	36.8	28
Matrimid	8.4	39.4	37
PDMS	2500	3.1	25
Matrimid	9	41.7	29
PEI	1.68	18.7	38
Matrimid	6.2	31	39
Ultem	1.46	39.5	
6FDA-ODA:DAM	54.1	23.5	
PMP	98.7	8.7	40
Matrimid	8.4	39.4	37
PSF	5.4	31	41
Matrimid	6.2	31	39
Ultem	1.46	39.5	
6FDA-ODA:DAM	54.1	23.5	
PMP	98.7	8.7	40
PSF	2.7	52	42
Ultem	1.5	38	43
Matrimid	9	32	
6FDA-DAM	390	24	
6FDA-ODA	14.4	44.1	8
PI	5.9	31.2	
PIM-1	3620	15.1	16
6FDA-ODA	14.4	44.1	35
PI	5.9	31.2	16
PSF	5.6	26.6	34
PVAc	2.44	34.9	32

© 2017 Macmillan Publishers Limited, part of Springer Nature. All rights reserved.

Supplementary Note 1: Modulation of MOF crystals.

Modulation of coordination chemistry in MOF synthesis arises from introducing a modulator, competing with the MOF's bridging ligands for coordination to the metal centers [1]. The modulator can act either to enhance crystal growth or to inhibit it. In the latter case, the modulator works as a capping agent and compete with the ligand for access to the metal cations, slowing nucleation and crystallization. The resulting modulated MOF structures become less defined and heterogeneous because of missing linkers, compensated by deprotonated modulator molecules [2].

The capping agents also prevent further assembly of the MOF network from the polydentate ligand, therefore, the particle crystal size decrease. The effects of modulation on the properties of MOFs have largely been as a result of change in the particle size, rather than specific surface chemistry [3].

Supplementary Note 2: Computational studies.

To gain insight into the adhesion processes between PIM-1 and UiO-66 metal-organic frameworks (MOFs), a series of simulation studies were conducted, using the Adsorption Locator and Forcite programs in Material Studio. PIM-1, UiO-66 and UiO-66-NH_2 were described with the universal force field (UFF) combined with QEq charges. Using the crystal structure of UiO-66 as a starting point, two types (A and B) of models for UiO-66 and UiO-66-NH_2 were built (Supplementary Figure 10). UiO-66-A and UiO-66-NH_2-A consist of 12 $Zr_6O_4(OH)_4$ cores and 127 linkers, whereas UiO-66-B and UiO-66-NH_2-B consist of 24 $Zr_6O_4(OH)_4$ cores and 169 linkers. UiO-66-A and UiO-66-NH_2-A feature corrugated surfaces, while UiO-66-B and UiO-66-NH_2-B have flat surfaces. The total charge is zero in all cases. The model we used for PIM-1 is shown in Supplementary Figure 11. Before doing adhesion-energy calculations, we optimized the structures of the separate PIM-1, UiO-66, and UiO-66-NH_2 models using the Forcite program. For the latter two models, heavy atoms in the $Zr_6O_4(OH)_4$ cores, terminal linkers at the truncation boundary, and carboxyl oxygen atoms of the linkers were fixed during the geometry optimizations to maintain the framework structure of UiO-66. Several plausible structures of adhesion complexes were generated with the Adsorption Locator program. The atoms at the target site for the sampling of PIM-1 configurations are shown in stick representation in Supplementary Figure 11. During Adsorption Locator calculations, the above-optimized geometries of the MOFs were kept fixed. USCF Chimera was used for visualizing molecules.

Supplementary Table 2 summarizes the calculated adhesion energies for UiO-66-A and UiO-66-NH_2-A. The adhesion energy of UiO-66-NH_2-A-1 (-72.2 kcal/mol) is significantly smaller than that of UiO-66-A-1 (-55.3 kcal/mol). This significant difference is attributable to the fact that the nitrile group and the oxygen atom of PIM-1 can form hydrogen bonds with the –NH_2 groups of UiO-66-NH_2 in UiO-66-NH_2-A-1; these hydrogen bonds are absent in UiO-66-A-1. However, the adhesion energies of UiO-66-NH_2-A-2 and UiO-66-NH_2-A-3 are not much different from that of UiO-66-A-1 because a smaller number of hydrogen bonds can be formed in in these cases. These results highlight the importance of H-bonding in the adhesion of PIM-1 and UiO-66-NH_2 on the corrugated surface. On the other hand, the adhesion energies for UiO-66-NH_2-B and UiO-66-B are nearly the same, as shown in Supplementary Table 3. This can be understood from the fact that no hydrogen bonds are formed (Supplementary Figure 12). The results obtained for UiO-66-B and UiO-66-NH_2-B indicate that the flat surface is less relevant to the enhancement of adhesion. Hence, the enhanced MOF/PIM-1 interfacial adhesion in the case of UiO-66-NH_2 should be primarily due to the H-bonding interactions at the corrugated surface.

© 2017 Macmillan Publishers Limited, part of Springer Nature. All rights reserved.

Supplementary Note 3. Bushell *et al.* have recently noted various trends of MMMs in terms of relative trade-offs in permeability and selectivity[12]. Many selectivity enhancements are seen with the addition of activated carbons or fused silica fillers[13]. The significant account of the various combinations of MOF MMMs collated by Seoane *et al.*[14] and also Rezakazemi *et al.*[15] was used to generate the comparative results in Figures 4 and Supplementary Figure 21. Additionally Kaliaguine and co-workers showed that amine-functional groups in synthesized MOF-199 increased the CO_2/CH_4 selectivity (up to 35%) in 6FDA–ODA polyimide MMMs[8]. Vankelecom and co-workers also reported ~50% selectivity increases in CO_2/CH_4 separation through the use of benzoic acid modulated amine functionalized UiO-66 particles, albeit with a single and high loading (30%) and a low-permeability polyimide matrix[16]. Gascon and co-workers reported the use of MOF nanosheets to increase selectivity by 35%, again over the base matrix of polyimide [17]. As is apparent in Seoane's review[14], these enhancements in selectivity are predominantly reported for MMMs (such as 6FDA–ODA, Matrimid or Pebax®) with permeabilities that are 1-2 orders of magnitude lower than what are possible with PIM class materials.

© 2017 Macmillan Publishers Limited, part of Springer Nature. All rights reserved.

Supplementary References

1 McGuire, C. V. & Forgan, R. S. The surface chemistry of metal–organic frameworks. *Chemical communications* 51, 5199-5217 (2015).
2 Shearer, G. C. *et al.* Defect Engineering: Tuning the Porosity and Composition of the Metal–Organic Framework UiO-66 via Modulated Synthesis. *Chemistry of Materials* 28, 3749-3761 (2016).
3 Stock, N. & Biswas, S. Synthesis of metal-organic frameworks (MOFs): routes to various MOF topologies, morphologies, and composites. *Chemical reviews* 112, 933-969 (2011).
4 Gómez-Gualdrón, D. A., Moghadam, P. Z., Hupp, J. T., Farha, O. K. & Snurr, R. Q. Application of consistency criteria to calculate BET areas of micro-and mesoporous metal–organic frameworks. *Journal of the American Chemical Society* 138, 215-224 (2015).
5 Furukawa, H. & Yaghi, O. M. Storage of hydrogen, methane, and carbon dioxide in highly porous covalent organic frameworks for clean energy applications. *Journal of the American Chemical Society* 131, 8875-8883 (2009).
6 Diring, S., Furukawa, S., Takashima, Y., Tsuruoka, T. & Kitagawa, S. Controlled multiscale synthesis of porous coordination polymer in nano/micro regimes. *Chemistry of Materials* 22, 4531-4538 (2010).
7 Hao, L., Liao, K.-S. & Chung, T.-S. Photo-oxidative PIM-1 based mixed matrix membranes with superior gas separation performance. *Journal of Materials Chemistry A* 3, 17273-17281 (2015).
8 Nik, O. G., Chen, X. Y. & Kaliaguine, S. Functionalized metal organic framework-polyimide mixed matrix membranes for CO 2/CH 4 separation. *Journal of Membrane Science* 413, 48-61 (2012).
9 Khan, M. M. *et al.* Cross-linking of polymer of intrinsic microporosity (PIM-1) via nitrene reaction and its effect on gas transport property. *European Polymer Journal* 49, 4157-4166 (2013).
10 Du, N., Dal-Cin, M. M., Robertson, G. P. & Guiver, M. D. Decarboxylation-induced cross-linking of Polymers of Intrinsic Microporosity (Pims) for membrane gas separation†. *Macromolecules* 45, 5134-5139 (2012).
11 Thomas, S., Pinnau, I., Du, N. & Guiver, M. D. Pure-and mixed-gas permeation properties of a microporous spirobisindane-based ladder polymer (PIM-1). *Journal of Membrane Science* 333, 125-131 (2009).
12 Bushell, A. F. *et al.* Gas permeation parameters of mixed matrix membranes based on the polymer of intrinsic microporosity PIM-1 and the zeolitic imidazolate framework ZIF-8. *Journal of Membrane Science* 427, 48-62 (2013).
13 Goh, P. S., Ismail, A. F., Sanip, S. M., Ng, B. C. & Aziz, M. Recent advances of inorganic fillers in mixed matrix membrane for gas separation. *Separation and Purification Technology* 81, 243-264 (2011).
14 Seoane, B. *et al.* Metal–organic framework based mixed matrix membranes: a solution for highly efficient CO 2 capture? *Chemical Society Reviews* 44, 2421-2454 (2015).
15 Rezakazemi, M., Amooghin, A. E., Montazer-Rahmati, M. M., Ismail, A. F. & Matsuura, T. State-of-the-art membrane based CO 2 separation using mixed matrix membranes (MMMs): an overview on current status and future directions. *Progress in Polymer Science* 39, 817-861 (2014).
16 Anjum, M. W. *et al.* Modulated UiO-66-Based Mixed-Matrix Membranes for CO2 Separation. *ACS applied materials & interfaces* 7, 25193-25201 (2015).
17 Rodenas, T. *et al.* Metal–organic framework nanosheets in polymer composite materials for gas separation. *Nature materials* 14, 48-55 (2015).
18 Ordoñez, M. J. C., Balkus, K. J., Ferraris, J. P. & Musselman, I. H. Molecular sieving realized with ZIF-8/Matrimid® mixed-matrix membranes. *Journal of Membrane Science* 361, 28-37 (2010).
19 Díaz, K., López-González, M., del Castillo, L. F. & Riande, E. Effect of zeolitic imidazolate frameworks on the gas transport performance of ZIF8-poly (1, 4-phenylene ether-ether-sulfone) hybrid membranes. *Journal of Membrane Science* 383, 206-213 (2011).
20 Song, Q. *et al.* Zeolitic imidazolate framework (ZIF-8) based polymer nanocomposite membranes for gas separation. *Energy & Environmental Science* 5, 8359-8369 (2012).
21 Lively, R. P. *et al.* A high-flux polyimide hollow fiber membrane to minimize footprint and energy penalty for CO 2 recovery from flue gas. *Journal of Membrane Science* 423, 302-313 (2012).
22 Wijenayake, S. N. *et al.* Surface cross-linking of ZIF-8/polyimide mixed matrix membranes (MMMs) for gas separation. *Industrial & Engineering Chemistry Research* 52, 6991-7001 (2013).
23 Bhaskar, A., Banerjee, R. & Kharul, U. ZIF-8@ PBI-BuI composite membranes: elegant effects of PBI structural variations on gas permeation performance. *Journal of Materials Chemistry A* 2, 12962-12967 (2014).
24 Li, T., Pan, Y., Peinemann, K.-V. & Lai, Z. Carbon dioxide selective mixed matrix composite membrane containing ZIF-7 nano-fillers. *Journal of Membrane Science* 425, 235-242 (2013).
25 Car, A., Stropnik, C. & Peinemann, K.-V. Hybrid membrane materials with different metal–organic frameworks (MOFs) for gas separation. *Desalination* 200, 424-426 (2006).

© 2017 Macmillan Publishers Limited, part of Springer Nature. All rights reserved.

26 Hu, J. *et al.* Mixed-matrix membrane hollow fibers of Cu3 (BTC) 2 MOF and polyimide for gas separation and adsorption. *Industrial & Engineering Chemistry Research* 49, 12605-12612 (2010).
27 Ge, L., Zhou, W., Rudolph, V. & Zhu, Z. Mixed matrix membranes incorporated with size-reduced Cu-BTC for improved gas separation. *Journal of Materials Chemistry A* 1, 6350-6358 (2013).
28 Duan, C. *et al.* Enhanced gas separation properties of metal organic frameworks/polyetherimide mixed matrix membranes. *Journal of Applied Polymer Science* 131 (2014).
29 Perez, E. V., Balkus, K. J., Ferraris, J. P. & Musselman, I. H. Mixed-matrix membranes containing MOF-5 for gas separations. *Journal of Membrane Science* 328, 165-173 (2009).
30 Arjmandi, M. & Pakizeh, M. Mixed matrix membranes incorporated with cubic-MOF-5 for improved polyetherimide gas separation membranes: Theory and experiment. *Journal of Industrial and Engineering Chemistry* 20, 3857-3868 (2014).
31 Hsieh, J. O., Balkus, K. J., Ferraris, J. P. & Musselman, I. H. MIL-53 frameworks in mixed-matrix membranes. *Microporous and Mesoporous Materials* 196, 165-174 (2014).
32 Adams, R., Carson, C., Ward, J., Tannenbaum, R. & Koros, W. Metal organic framework mixed matrix membranes for gas separations. *Microporous and Mesoporous Materials* 131, 13-20 (2010).
33 Bae, T.-H. & Long, J. R. CO 2/N 2 separations with mixed-matrix membranes containing Mg 2 (dobdc) nanocrystals. *Energy & Environmental Science* 6, 3565-3569 (2013).
34 Su, N. C. *et al.* Enhanced permeation arising from dual transport pathways in hybrid polymer–MOF membranes. *Energy & Environmental Science* (2016).
35 Smith, S. J., Ladewig, B. P., Hill, A. J., Lau, C. H. & Hill, M. R. Post-synthetic Ti exchanged UiO-66 metal-organic frameworks that deliver exceptional gas permeability in mixed matrix membranes. *Scientific reports* 5 (2015).
36 Japip, S., Wang, H., Xiao, Y. & Chung, T. S. Highly permeable zeolitic imidazolate framework (ZIF)-71 nano-particles enhanced polyimide membranes for gas separation. *Journal of Membrane Science* 467, 162-174 (2014).
37 Shahid, S. & Nijmeijer, K. Performance and plasticization behavior of polymer–MOF membranes for gas separation at elevated pressures. *Journal of membrane science* 470, 166-177 (2014).
38 Ren, H., Jin, J., Hu, J. & Liu, H. Affinity between metal–organic frameworks and polyimides in asymmetric mixed matrix membranes for gas separations. *Industrial & Engineering Chemistry Research* 51, 10156-10164 (2012).
39 Chen, X. Y., Hoang, V.-T., Rodrigue, D. & Kaliaguine, S. Optimization of continuous phase in amino-functionalized metal–organic framework (MIL-53) based co-polyimide mixed matrix membranes for CO 2/CH 4 separation. *Rsc Advances* 3, 24266-24279 (2013).
40 Abedini, R., Omidkhah, M. & Dorosti, F. Highly permeable poly (4-methyl-1-pentyne)/NH 2-MIL 53 (Al) mixed matrix membrane for CO 2/CH 4 separation. *RSC Advances* 4, 36522-36537 (2014).
41 Seoane, B., Sebastián, V., Téllez, C. & Coronas, J. Crystallization in THF: the possibility of one-pot synthesis of mixed matrix membranes containing MOF MIL-68 (Al). *CrystEngComm* 15, 9483-9490 (2013).
42 Zornoza, B. *et al.* Functionalized flexible MOFs as fillers in mixed matrix membranes for highly selective separation of CO 2 from CH 4 at elevated pressures. *Chemical communications* 47, 9522-9524 (2011).
43 Bae, T. H. *et al.* A High-Performance Gas-Separation Membrane Containing Submicrometer-Sized Metal–Organic Framework Crystals. *Angewandte Chemie International Edition* 49, 9863-9866 (2010).
44 Zhang, Y., Balkus, K. J., Musselman, I. H. & Ferraris, J. P. Mixed-matrix membranes composed of Matrimid® and mesoporous ZSM-5 nanoparticles. *Journal of Membrane Science* 325, 28-39 (2008).
45 Pechar, T. W., Tsapatsis, M., Marand, E. & Davis, R. Preparation and characterization of a glassy fluorinated polyimide zeolite-mixed matrix membrane. *Desalination* 146, 3-9 (2002).
46 Huang, Z., Li, Y., Wen, R., May Teoh, M. & Kulprathipanja, S. Enhanced gas separation properties by using nanostructured PES-Zeolite 4A mixed matrix membranes. *Journal of applied polymer science* 101, 3800-3805 (2006).
47 Jha, P. & Way, J. D. Carbon dioxide selective mixed-matrix membranes formulation and characterization using rubbery substituted polyphosphazene. *Journal of Membrane Science* 324, 151-161 (2008).
48 Pechar, T. W. *et al.* Fabrication and characterization of polyimide–zeolite L mixed matrix membranes for gas separations. *Journal of Membrane Science* 277, 195-202 (2006).
49 Li, Y., Chung, T. S. & Kulprathipanja, S. Novel Ag+-zeolite/polymer mixed matrix membranes with a high CO2/CH4 selectivity. *AIChE Journal* 53, 610-616 (2007).
50 Duval, J. M. *et al.* Preparation of zeolite filled glassy polymer membranes. *Journal of Applied Polymer Science* 54, 409-418 (1994).
51 Amooghin, A. E., Omidkhah, M. & Kargari, A. Enhanced CO2 transport properties of membranes by embedding nano-porous zeolite particles into Matrimid® 5218 matrix. *RSC Advances* 5, 8552-8565 (2015).

© 2017 Macmillan Publishers Limited, part of Springer Nature. All rights reserved.

52 Rabiee, H., Alsadat, S. M., Soltanieh, M., Mousavi, S. A. & Ghadimi, A. Gas permeation and sorption properties of poly (amide-12-b-ethyleneoxide)(Pebax1074)/SAPO-34 mixed matrix membrane for CO 2/CH 4 and CO 2/N 2 separation. *Journal of Industrial and Engineering Chemistry* 27, 223-239 (2015).
53 Hillock, A. M., Miller, S. J. & Koros, W. J. Crosslinked mixed matrix membranes for the purification of natural gas: effects of sieve surface modification. *Journal of membrane science* 314, 193-199 (2008).
54 Murali, R. S., Ismail, A. F., Rahman, M. A. & Sridhar, S. Mixed matrix membranes of Pebax-1657 loaded with 4A zeolite for gaseous separations. *Separation and Purification Technology* 129, 1-8 (2014).

© 2017 Macmillan Publishers Limited, part of Springer Nature. All rights reserved.